Volume 12
Number 30
14 August 2024
Pages 11195–11660

Journal of Materials Chemistry C

Materials for optical, magnetic and electronic devices

rsc.li/materials-c

ISSN 2050-7526

ROYAL SOCIETY OF CHEMISTRY

PAPER

Massimiliano Arca, Giuseppe Sforazzini *et al.*
Unveiling the significance of adduct formation between thiocarbonyl Lewis donors and diiodine for the structural organization of rhodanine-based small molecule semiconductors

Journal of Materials Chemistry C

ROYAL SOCIETY OF CHEMISTRY

PAPER

View Article Online
View Journal | View Issue

Cite this: J. Mater. Chem. C, 2024, 12, 11352

Unveiling the significance of adduct formation between thiocarbonyl Lewis donors and diiodine for the structural organization of rhodanine-based small molecule semiconductors†

Anna Laura Sanna, [a] Simone Acca,[a] Enrico Podda, [b] Antonello Mascia, [c] Anna Pintus, [a] M. Carla Aragoni, [a] Vito Lippolis, [a] Carlo Ricci,[d] Piero Cosseddu, [c] Massimiliano Arca *[a] and Giuseppe Sforazzini *[a]

Rhodanine vinyl bithiophene (**BTR**) was synthesized and characterized both spectroscopically and structurally. The reaction of **BTR** with molecular iodine led to the 1 : 1 "spoke" adduct **BTR·I$_2$**, formed by interaction of the rhodanine thiocarbonyl group with a diiodine (I_2) molecule. The elongation of the I–I bond in the adduct with respect to solid-state I_2 and the Raman response in the low-energy region (ν = 150 cm^{-1}) clearly indicate **BTR·I$_2$** to be a weak CT adduct. Hybrid-DFT calculations showed that the adduct formation narrowed the HOMO–LUMO gap in **BTR·I$_2$** as compared to **BTR**, while the extended network of secondary interactions, including type-I halogen bonds (XB), results in the formation of an extended 3D network. As a consequence, the room temperature conductivity of **BTR·I$_2$** increased with respect to **BTR**, testifying for a more efficient molecular packing for charge percolation, with the formation of charge carriers in the crystal being facilitated by the presence of I_2. It is worth noting that the single-crystal junction device operates at room temperature, in air, and no variation of conductivity over time was observed, indicating that no loss of diiodine occurred during measurements. These results clearly indicate the formation of thiocarbonyl–diiodine CT adducts and their potential as a solid additive for modulating the organization of small molecule semiconductors.

Received 1st May 2024,
Accepted 17th June 2024

DOI: 10.1039/d4tc01791a

rsc.li/materials-c

Introduction

The molecular organization of π-conjugated compounds in the solid-state plays a crucial role in organic electronics.[1–3] Intermolecular interactions, including π–π stacking, dipole–dipole, and charge transfer interactions, significantly influence the arrangement of molecules, thereby defining pathways for charge percolation.[4–7] Understanding and controlling these interactions is essential for improving the energy efficiency, stability, and overall performance of organic electronic devices.

Over the past decade, there has been an increasing interest in the development of a class of π-conjugated compounds commonly referred to as "small molecules" (SMs).[8–10] These compounds are currently widely investigated for their potential in creating n-type semiconductor materials for highly efficient and sustainable organic solar cells (OSCs), among other applications.[9–13] The typical design of a SM consists of a polycyclic aromatic π-system arranged in a linear or fused fashion, along with solubilizing side chain and electron directing functionality (Fig. 1). Widespread research efforts have been devoted to enhancing the efficiency of OSCs by thoughtfully tuning the energy level of the π-conjugated compounds and carefully selecting solubilizing chains to control their arrangement in the solid state once they are processed from solution.[14–16] However, it is essential to note that an inappropriate choice of solubilizing groups can have a detrimental impact on the performance of an optoelectronic device. This occurs because the lateral side chains might promote molecular assemblies with good local charge mobility but an overall modest charge carrier percolation.[17–21] Exploring post-synthetic approaches for controlling molecular organization is of particular interest. Common strategies involve the use of processing

[a] Department of Chemical and Geological Sciences, University of Cagliari, S.P. no. 8 km 0.700, Monserrato 09042, Cagliari, Italy.
E-mail: giuseppe.sforazzini@unica.it, marca@unica.it
[b] Centro Servizi di Ateneo per la Ricerca - CeSAR, University of Cagliari, S.P. no. 8 Km 0.700, Monserrato 09042, Cagliari, Italy
[c] Department of Electrical and Electronic Engineering, University of Cagliari, Piazza d'Armi, Cagliari 09123, Italy
[d] Department of Physics, University of Cagliari, S.P. no. 8 Km 0.700, 09042, Monserrato, CA, Italy

† Electronic supplementary information (ESI) available: Synthetic procedures, NMR spectra, XRD analyses, computational details. CCDC 2341835 and 2341836. For ESI and crystallographic data in CIF or other electronic format see DOI: https://doi.org/10.1039/d4tc01791a

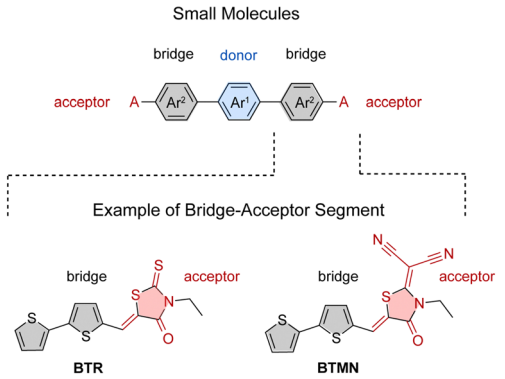

Fig. 1 Schematic representation of the molecular structure of small molecule semiconductors (top). Selected representative examples of the bridge–acceptor molecular structure segment (bottom). **BTR** = bithiophene vinyl rhodanine; **BTMN** = bithiophene vinyl rhodanine malonitrile.

additives in the solution of organic semiconductors during the drying process, and thermal post-treatment of the formed thin films. Based on their distinct properties and effects, additives can be categorized into two categories: solvent additives and solid additives. The first category typically consists of solvents that primarily impact the solution state and evaporation dynamics in the film formation process. These additives have a higher boiling point as compared to the main solvent, leading to a slower evaporation rate during the film preparation, thus allowing for fine-tuning of the film crystallinity, as well as the phase separation in the case of blends.[15,22–25]

The second category, solid additives, operates distinctively from their solvent counterparts, first because they alter the intermolecular interaction among π-conjugated compounds, and second because they are incorporated into the films, so in principle they do not require high temperature for their removal.[26–28] Such a scenario is particularly interesting as it avoids the risk of film degradation which inevitably leads to a reduction in device performance. Examples of solid additives include 7-dibromo-9,9-dimethyl fluorene (DBDMF), hydroxymethylpyrimidine derivatives, 9-fluorenone-1-carboxylic acid (FCA), 2-benzylidene-1-indene-1,3-dione and its derivatives, and diiodine.[26–30] The latter additive is particularly intriguing because it is commonly employed also as a p-type chemical dopant for both small molecules and π-conjugated polymers, contributing to the enhancement of charge carriers in the semiconductor layer.[29,30] However, the optimal generation of charge carriers relies heavily on the homogeneous distribution of the dopant throughout the material. To achieve this objective, various parameters must be carefully tuned during the film deposition process. Studies have demonstrated that employing higher temperatures is advantageous for this purpose.[29] Consequently, the use of a solid dopant may prove to be less energy-effective if heat must be applied during the fabrication of optoelectronic devices. As a possible solution to this problem, our vision is to leverage the terminal functionality of semiconductors as coordination points for solid additives/dopants, so to reach a homogeneous distribution at the molecular level in the materials also at room temperature. In this context, intermolecular charge-transfer (CT)[31] and σ-hole interactions,[32] such as hydrogen, halogen, and chalcogen bonding interactions,[33] are very promising to establish directional secondary bonds between semiconducting compounds and solid additives. In particular, contrary to carbonyl groups (C═O), chalcocarbonyl functionality C═Ch (Ch = S, Se) is known to promote intermolecular CT with I_2.[31] At the same time, the C═Ch unit is of common occurrence in the terminal unit of SMs as it is intrinsically included in the molecular architecture of rhodanine electron-directing groups.[9,11–13] To the best of our knowledge, no examples of C═Ch···I_2 interactions in the rhodanine functionality and in the presence of π-conjugated compounds have been reported in the past. Therefore, we have focused our attention on investigating C═Ch···I_2 bond formation in a model compound consisting of a π-conjugated segment directly connected to a rhodanine functionality. In this work, we report on the synthesis and structural and spectroscopic characterization of a bithiophene derivative featuring a *N*-ethylrhodanine (**BTR**, Fig. 1), and its CT adduct with molecular iodine. By utilizing a single crystal junction set-up, the effect of solid-state molecular organization on charge percolation through the crystals of the prepared compounds and adducts is investigated.

Results and discussion

Design and synthesis

We designed a bithiophene π-conjugated backbone decorated with a rhodanine electron-withdrawing group as a model of the bridge–acceptor segment of a SM semiconductor (Fig. 1). The bithiophenic segment was deliberately incorporated in the design to mimic the behaviour of the bridging linker between a hypothetical central core of a small molecule and the acceptor terminal group. Thus, the bithiophene moiety serves a dual purpose: first, it helps establish a reasonable electronic density in proximity to the electron-withdrawing group (rhodanine), and second, it functions as a means to verify the absence of side reactions, such as halogenation in positions 2 and 3, when the compounds undergo treatment with halogens. The synthetic pathway of the model compound bithiophene vinyl rhodanine (**BTR**) is depicted in Scheme 1. **BTR** was synthesized by Vilsmeier reaction[34] followed by Knoevenagel condensation.[35] Commercially available 2,2′-bithiophene (**BT**) underwent an initial reaction with phosphorus oxychloride (V), $POCl_3$, and dimethylformamide (DMF) in 1,2-dichloroethane (1,2-DCE), resulting in quantitative yield of 2,2′-bithiophene-5-carbaldehyde (**BTA**).

Subsequently, the obtained acylated product was reacted with *N*-ethylrhodanine, in the presence of piperidine and ethanol, to give the desired product in quantitative yields.

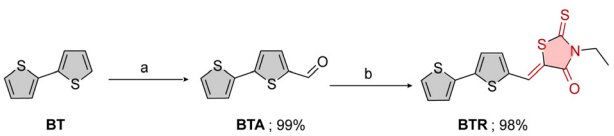

Scheme 1 (a) $POCl_3$ (i), DMF (ii), 1,2-DCE, reflux (83 °C), 24 h; (b) 3-ethyl-2-thioxo-1,3-thiazolidin-4-one, piperidine, ethanol, reflux (78 °C), 24 h.

BTR was then treated with I_2 to form CT adducts through the interaction of the rhodanine C═S functionality and I_2.

X-ray diffraction analysis

The reactions between thiocarbonyl donors and I_2 allow for the formation of a variety of products, including simple CT "spoke" adducts C═S···I–I, "extended" CT adducts C═S···I–I–(I–I)$_n$, iodonium compounds C═S···I^+···S═C, in addition to donor oxidation products such as $[C–S–S–C]^{2+}$ dications.[31] Cationic products can be counterbalanced by discrete or extended (poly)iodides with the general formula $[I_{2m+n}]^{n-}$ (n, $m > 0$), such as $[I_4]^{2-}$, $[I_5]^-$, and $[I_7]^-$, with the largest reported so far being the ferrocenium salt of $[I_{29}]^{3-}$.[36,37] To investigate the potential scenarios involving rhodanine-containing thiophene derivatives, **BTR** and I_2 were made to react under various reaction conditions, systematically changing both the solvents and the molar ratios of reactants. Single crystals of **BTR** were grown by slow evaporation of an ethanol solution (Table S1, ESI†). The molecular unit is nearly planar except for the ethyl substituent at the rhodanine ring (Fig. 2a). Notably, the rhodanine ring shows the endocyclic sulfur atom periplanar with respect to the central thiophene ring, while the terminal thiophene is disordered over two positions, periplanar (64%) and antiperiplanar (36%) with respect to the central ring. Parallel **BTR** units (angle between the molecular planes 1.7°) are packed in a head-to-tail fashion based on π–π slipped stacking interactions between rhodanine and the terminal thiophene rings (intercentroid distance = 3.68 Å considering the major component) to form a pile developing along the [001] direction (Fig. 2b). Parallel piles pack along the [010] direction through interactions involving the ethyl substituents and the thiophene and the rhodanine rings. By either diffusion of diiodine vapors into a **BTR** hexane solution or direct mixing of hexane solutions of **BTR** and I_2, a single type of product was isolated, identified as **BTR·I$_2$** by single-crystal X-ray diffraction analysis, and consisting of a CT "spoke" adduct showing a (C═)S···I–I linear moiety [S1···I1, 2.7576(5); I1–I2, 2.8067(4) Å; S1–I1–I2, 164.70(1)°; Fig. 2c]. Analogous to the crystal structure of **BTR**, the disorder of the terminal thiophene was modelled over two sites with atomic occupancies of 85 : 15 with the predominance of the antiperiplanar conformation. Interestingly, the planarity observed for the **BRT** units in its crystal structure is retained in the CT adduct with I_2. As typical of CT interactions, the transfer of electron density from the thiocarbonyl donor to I_2 results in a slight elongation of the C═S bond [C1–S1 = 1.632(2) and 1.666(1) Å in **BTR** and **BTR·I$_2$**, respectively]. Accordingly, the I–I bond in **BTR·I$_2$** is elongated as compared to free I_2 [I1–I2 = 2.806(1) and 2.715(6) Å in **BTR·I$_2$** and in the free I_2,[38] respectively], as a consequence of the CT to the I_2 antibonding σ* MO. Accordingly, the I–I bond length in **BTR·I$_2$** corresponds to a Pauling bond order of 0.691.[39] The strength of the CT interaction in **BTR·I$_2$** is weaker than the average of the related CT adducts deposited in the Cambridge Structural Database (CSD) between thiocarbonyl donors embedded in pentatomic rings and I_2 featuring a S···I–I moiety [angle larger than 170°, 44 hits; S···I and I–I average distances = 2.695(7) and 2.879(5) Å, respectively]. The weakness of the interaction can be attributed to the presence of the electron withdrawing carbonyl group in the rhodanine ring.

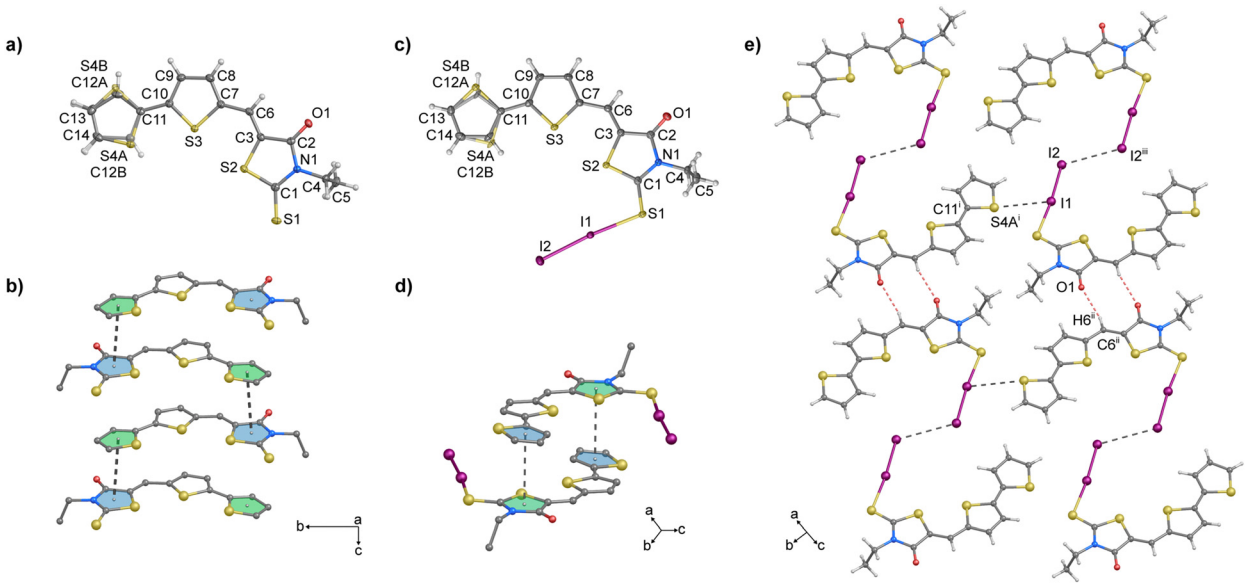

Fig. 2 (a) Ellipsoid plot and atom labelling scheme of compound **BTR**. The terminal thiophene ring is disordered over two positions with fractional occupancies 64 : 36. (b) Intermolecular interactions in the crystal packing of compound **BTR** (intercentroid distance of 3.68 Å). The minor component of the disordered moiety was omitted for clarity. (c) Ellipsoid plot and atom labelling scheme of compound **BTR·I$_2$**. The terminal thiophene ring is disordered over two positions with fractional occupancies 85 : 15. (d) π–π stacking interactions between pairs of **BTR·I$_2$** units featuring an intercentroid distance of 3.67 Å when considering the most abundant position of the disordered terminal thiophenyl moiety. (e) View along the [101] direction of a portion of a ribbon motif found in the crystal structure of **BTR·I$_2$** (see the text for a description of weak interactions). Ellipsoids were drawn at the 50% probability level. Hydrogen atoms were omitted for clarity in (b) and (d). Symmetry operations: ^{i} = 1 + x, 1 + y, +z; ^{ii} = 1 − x, 2 − y, 2 − z; ^{iii} = 1 − x, 1 − y, −z. See Tables S2–S5 (ESI†) for selected bond angles (°) and distances (Å).

The bond distances and angles in the >C═S···I–I fragment of **BTR·I$_2$** strictly recall those observed in the adduct (mdth)·I$_2$ (mdth = 1,5,5-trimethyl-2-thiohydantoin) [S···I 2.818(2), I–I 2.795(1) Å, S···I–I 178.03(3)°].[40] It is worth noting that the S···I and I–I relative bond distances in the S···I–I moiety clearly fall within the correlation proposed by Devillanova for linear three-body systems A–B–C involving either halogens, X–X–X (X = Br, I), or halogen(s) and chalcogen(s) atoms, Ch–X–Y, X–Ch–Y, and Ch–X–Ch (Ch = S, Se; X = Y = Cl, Br, I; X = I, Y = Cl, Br, I), which correlates the relative elongations δ_1 and δ_2 of the two interatomic distances with respect to the sum of the relevant covalent radii (Fig. S1 in the ESI†). Pairs of planar adduct units show π–π stacking interactions between the rhodanine ring of one unit and the terminal thiophene ring of a symmetry related one (intercentroid distance 3.67 Å; Fig. 2d). Dimers formed by adjacent pairs interact through C–S···I and C–H···O weak contacts, the latter defining a $R_2^2(10)$ hydrogen bonding motif as the result of two interacting symmetry-related rhodanine groups [C11^{i}–S4 = 1.721(2); S4A^{i}···I1 = 3.660(1) Å; C11^{i}–S4A^{i}···I1 = 172.66(8); C1–S1 = 1.666(2); C6–H6 = 0.95 Å; H6^{ii}···O1 = 2.34; C6^{ii}···O1 = 3.210(3) Å; C6^{ii}–H6^{ii} ···O1 = 151°; ^{i} = 1 + *x*, 1 + *y*, +*z*; ^{ii} = 1 − *x*, 2 − *y*, 2 − *z*; Fig. 2e and S2 in the ESI†]. In addition, the terminal I$_2$ units show very weak I···I contacts, close to the sum of the relevant van der Waals radii, with a topology typical of bent type-I halogen bonds (XB) [I2···I2^{iii} = 4.1267(5) Å; I1–I2···I2^{iii} = 124.57(1)°; ^{iii} = 1–*x*, 1–*y*, –*z*; Fig. 2e].

Raman spectroscopy

Raman spectroscopy is a sensitive technique providing structural information on dihalogens, interhalogens, and (inter)-polyhalides.[41] In particular, in "spoke" I$_2$-adducts the extent of the elongation of perturbed diiodine is reflected in the shifting of the Raman peak due to the I–I σ_g stretching vibration. Molecular iodine (bond order n_{I-I} = 1) shows a peculiar peak at 214.5 cm^{-1} in the gas phase, due to the I–I stretching vibration.[42–45] The same vibration can be envisaged in the range 203–211 cm^{-1} in low-polar organic solvents.[45] Accordingly, nearly monomeric I$_2$ trapped in solid Kr displayed a distinct Raman band at 210.8 cm^{-1} at 32 K.[44] In crystalline I$_2$, two molecular units are present in the unit cell, and two vibrations can be envisaged, attributed to the in-phase (A_g, 180 cm^{-1}) and out-of-phase (B_{3g}, 189 cm^{-1}) stretching modes.[46,47] In solid state I$_2$ at room temperature, only the former band is often observed, so that I$_2$ is reported to feature a single Raman band.[45,48] In molecular systems containing perturbed diiodine (n_{I-I} < 1) the weakening of the I–I bond is reflected in a linearly dependent shift of the Raman A_g band toward lower wavenumbers. The Raman spectrum of **BTR·I$_2$** shows a single peak at 150 cm^{-1} (Fig. S3 in the ESI†), clearly absent in the Raman spectrum of **BTR**. The shift of this peak (about 30 cm^{-1}) with respect to the peak observed for solid I$_2$, together with the moderate elongation of the I–I bond, classifies **BTR·I$_2$** as a weak CT adduct (n_{I-I} > 0.6).[49] In fact, the Raman shift recorded for **BTR·I$_2$** falls within the linear correlation between the measured Raman frequency and the I–I bond distances reported for weak I$_2$ CT adducts.[49]

Computational study

To better understand the reactivity of **BTR** towards diiiodine, a set of theoretical calculations were performed on both **BTR** and its 1:1 diiodine CT adduct. Based on comparative investigations reported previously,[50,51] the hybrid mPW1PW[52] functional was paralleled by Schäfer, Horn and Ahlrichs split-valence basis sets including polarization functions (SVP),[53] in the formulation of Weigend (def2-SVP)[54] for all atoms except iodine, for which the LANL08(d)[55] basis set including relativistic effective core potentials (RECPs) was adopted. Over the past few decades, the interaction of chalcogen donors with diiodine has been described by using two apparently opposite descriptions. Traditionally, this interaction was interpreted on the basis of an orbital-mixing model as a charge-transfer (CT) interaction between the Lewis base **L**, featuring a lone pair of electrons (LP) on the donor atom, and the I$_2$ Lewis acid, featuring a σ* antibonding molecular orbital located along the I–I bond, so that the CT results in a lowering of the I–I bond order and an elongation of the bond as compared to that of unperturbed I$_2$.[31,43,48]

More recently, the same type of interactions has been considered to be governed by the anisotropy of electrostatic potential on the interacting halogen atom, whose charge depletion sites (σ-holes),[32] located opposite to the I–I bond in I$_2$ (Fig. 3b), would orient the halogen towards more nucleophilic sites in the organic molecule, *i.e.* those displaying a more negative electrostatic potential. In this context, the spoke adduct **L**·I$_2$ has been considered as the result of a halogen bond (XB)[56,57] interaction between the I$_2$ XB donor and the **L** acceptor.[58] Recent theoretical studies carried out often at the DFT level have agreed that σ-hole interactions result from different contributions. Energy decomposition analyses (EDAs) have shown that the energy of σ-hole interactions can be decomposed into an electrostatic term and an MO-mixing

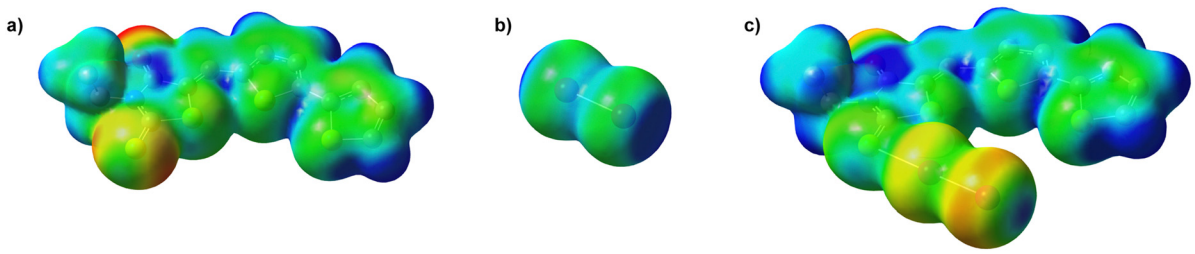

Fig. 3 Molecular electrostatic potential (MEP) mapped on the electron density surface (5 × 10^{-3} |e| bohr^{-3}) in **BTR** (a; periplanar conformation), I$_2$ (b), and **BTR·I$_2$** (c; periplanar conformer). MEP range −0.05 (red) – +0.05 (blue) a.u. Hydrogen atoms were omitted for clarity.

term,[59,60] in addition to dispersion.[61] The relative weight of each contribution depends largely on the nature of the involved groups, so that the nature of the σ-hole interactions spans from almost purely ionic, especially at longer distances, to largely covalent, in which case a three-body system, featuring complementary bond orders, can be envisaged.

With the aim to get an insight into the interaction between **BTR** and I_2, DFT calculations were carried out on the isolated **BTR** and I_2 molecules, and the **BTR·I$_2$** ''spoke'' adduct (see Tables S6–S8 in the ESI† for the orthogonal Cartesian coordinates in the optimized geometries). As described above, the crystal structure of **BTR** shows the terminal thiophene ring disordered over the two possible planar and antiperiplanar conformations. Both planar conformers were optimized in the gas phase showing a negligible total electronic energy difference (0.8 kcal mol^{-1}), thus justifying the presence of both conformers in the crystal structure. In Table 1, a selection of the natural charges[62–64] Q calculated for **BTR** at the optimized geometry is reported (see Tables S9–S11 for a full list in the ESI†). While thiophene and the rhodanine endocyclic S-atoms are positively charged, the rhodanine thiocarboxylic sulfur atom features a small negative charge. The Kohn–Sham (KS) HOMO and HOMO-1 calculated for **BTR** (Fig. S4 in the ESI†), very close in energy to each other (ε = –6.344 and –6.542 eV, respectively), show a significant contribution from the exocyclic S-atom. In particular, HOMO-1 is a 3p lone pair of electrons lying on the molecular plane. Therefore, the frontier MO composition and the natural population analysis (NPA)[62–64] indicate the exocyclic sulfur atom of the rhodanine ring as the preferred donor site towards I_2 in a CT interaction. On the other hand, Fig. 3a shows the electrostatic potential calculated for **BTR**, mapped on the electron density, clearly showing that the most negative electrostatic potential regions on the sulfur electron density are located on the molecular plane, in accordance with the structural data collected for **BTR·I$_2$**. Thus, the two limit views of MO interpretation and electrostatic potential map converge to the same result. Indeed, the regions on the sulfur atom showing the largest negative electrostatic potential coincide with those where the lobes of KS-HOMO-1 isosurfaces are located (see Fig. S5 in the ESI†).

The geometry of the 1 : 1 ''spoke'' adduct **BTR·I$_2$** was successfully optimized (Fig. S6 in the ESI†), with the diiodine unit lying on the molecular plane, in agreement with the structural data discussed above. A very good agreement between calculated and experimental bond lengths and angles was found. In particular, the interaction between the thiocarbonyl rhodanine group and diiodine shows metric parameters (C═S, 1.661; S···I, 2.951; I–I, 2.780 Å; S···I–I, 173.2°), close to those determined by single crystal X-ray diffraction analysis (see above). This notwithstanding, the optimized I–I bond distance is slightly longer than the experimental value (by 0.027 Å), suggesting a modest underestimation of the CT interaction. The moderate elongation of the I–I bond distance d_{I-I} in the adduct as compared with that optimized at the same level of theory for I_2 (Δd_{I-I} = 0.114 Å) is in agreement with the weak nature of the interaction. The interaction energy in the ''spoke'' adduct associated with the orbital mixing and CT can be evaluated by means of a second order perturbation theory analysis of the Fock matrix in the Natural Bond Orbital basis at the optimized geometry. This is achieved by examining all possible interactions between occupied (donor) NBOs and virtual (acceptor) non-Lewis NBOs and evaluating their interaction energy by means of the second order perturbation theory.[64] For each donor NBO (i) and acceptor NBO (j), the associated stabilization energy E_{CT} can be estimated as

$$E_{CT} = q_i \cdot F(i,j)/(\varepsilon_j - \varepsilon_i)$$

where q_i is the donor orbital occupancy, ε_j and ε_i are diagonal elements and $F(i,j)$ is the off-diagonal NBO Fock matrix element. In the case of **BTR·I$_2$**, the donor orbital is represented almost entirely (96.2%) by the filled bonding NBO localized on the exocyclic sulfur (i = 6) and the acceptor orbital by the antibonding NBO (j = 350), localized on the atoms I1 and I2 (54.10% and 45.90%, respectively) and antibonding with respect to the I–I bond. This interaction is calculated to be relatively small [E_{CT} = 31.4 kcal mol^{-1}; $F(6,350) = 7.2 \cdot 10^{-2}$ a.u.; $\Delta\varepsilon$ = 0.20 a.u.]. Accordingly, a NPA carried out on **BTR·I$_2$** at the optimized geometry (Table 1) reveals that the interaction led to a charge-transfer ΔQ_{CT} = 0.192 $|e|$ from the organic donor to the diiodine unit. The additional charge on I_2 is transferred in particular to the terminal iodine atom, which shows a remarkably negative natural charge (Q_I = –0.183 $|e|$).

As a consequence of the CT, the I–I Wiberg bond[65] index in the I_2 unit is lowered to 0.793, which is slightly larger than the value calculated from the structural data using Pauling's equation.

This is consistent with the weak adduct nature of the **BTR·I$_2$** adduct, evidenced by the optimized metric parameters (see above) and experimentally confirmed by Raman spectroscopy (see above). The molecular electron density mapped on the density surface in **BTR·I$_2$** clearly shows the most negative potential on the most electronegative oxygen atoms, in accordance with the NPA (Fig. 3c). It is worth noting that the terminal iodine atom in the adduct displays a distribution of the electrostatic potential pointing to a σ-hole topology, in perfect agreement with the long XB interactions connecting the stacks of **BTR·I$_2$** in the solid state, responsible for the 3D lattice dimensionality.

Table 1 Selected natural charges Q ($|e|$) calculated at the optimized geometry for **BTR** and **BTR·I$_2$**. Atom labelling scheme as in Fig. 2a and b. Values refer to the conformer with the thiophene rings in the periplanar conformation

Q	**BTR**	**BTR·I$_2$**
O1	−0.591	−0.581
N1	−0.502	−0.491
S1	−0.064	−0.020
S2	0.374	0.417
S3	0.430	0.445
S4	0.430	0.439
I1	—	−0.028
I2	—	−0.183

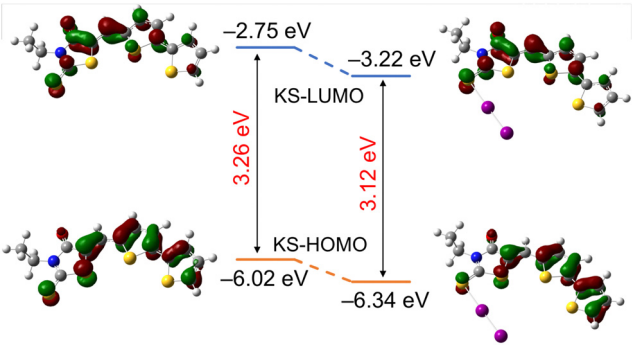

Fig. 4 Kohn–Sham frontier orbital energy levels for **BTR** (left) and **BTR·I$_2$** (right). Color: carbon, gray; nitrogen, blue; oxygen, red; sulfur, yellow; hydrogen, white. Cutoff value = 0.05 |e|.

Although Koopmans' theorem cannot be applied to density functional theory, the Kohn–Sham eigenvalues can be considered as useful parameters[66] in evaluating the variations in the HOMO–LUMO energy gap induced by the interaction of **BTR** with I_2. In fact, the gas-phase $\Delta\varepsilon_{HL}$ HOMO–LUMO energy gap is in good agreement with the band gap of small π-conjugated compounds.[57,67] In the case of **BTR** and **BTR·I$_2$** $\Delta\varepsilon_{HL}$ values of 3.26 and 3.16 eV are calculated (Fig. 4), falling within the range −2.5 ∼ −4.0 eV, typical of a small organic semiconductor.[67] It is noteworthy that the case of **BTR** clearly demonstrates how I_2-adduct formation can efficiently reduce the HOMO–LUMO energy gap in the resulting adducts compared to the pristine substrates. The case of study shows that this strategy holds not only when Lewis donors with a large Mulliken hardness are considered, as in the case of N-donors,[51] but also when softer S-donors are considered, as in the case of **BTR**. Finally, a vibrational analysis carried out on **BTR·I$_2$** confirms the attribution of the Raman peak at 150 cm^{-1} as due to the stretching of the perturbed I_2 unit.

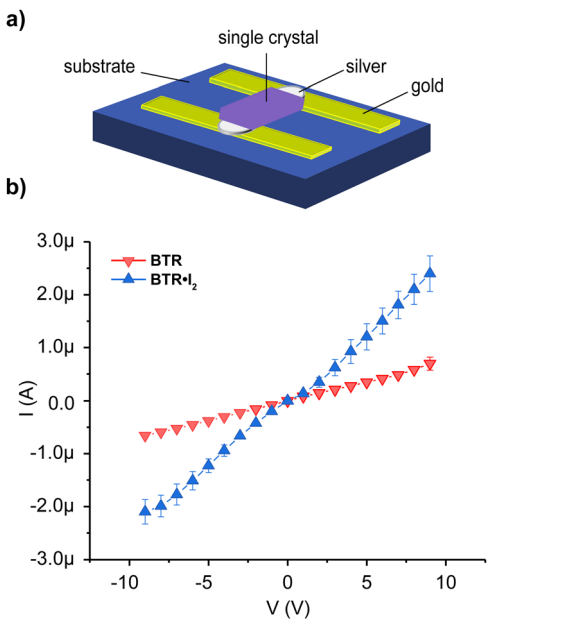

Fig. 5 (a) Device architecture for single-crystal electrical characterization. (b) Average current–voltage plots of **BTR** (red) and **BTR·I$_2$** (blue).

Single crystal electrical characterization

To investigate the impact of the molecular organization, induced by the thiocarbonyl–diiodine interactions, on the charge transport properties of the bulk material, we fabricated single crystal junction devices (see the ESI† for details). Single crystals of **BTR** and **BTR·I$_2$** were carefully transferred to the top of a glass substrate grafted with two gold pads. Each crystal was disposed to bridge the two electrodes, and a droplet of silver paste was applied in each crystal–metal junction to obtain a more stable electrical contact (Fig. 5a). In order to evaluate the stability and the reproducibility of the measurements, the two devices were measured on two different days and each measuring run was cycled five times. The average results of the electrical characterization are reported in Fig. 5b. From the reported plots we clearly observe that the different runs of measurements are very reproducible, as demonstrated by the limited standard deviation (see error bars) and, most importantly, that the **BTR·I$_2$** adduct is characterized by a much higher conductivity with respect to the crystals of the pristine **BTR**. It is worth noting that the distance between the two electrodes was kept constant in the two sets of devices, and that the crystals have been properly selected to have comparable geometrical dimensions, *i.e.* width and height. The enhanced electrical current of the adducts might suggest that molecules have adopted a more efficient packing for charge percolation, and at the same time diiodine may have facilitated the formation of charge carriers in the crystal. It is noteworthy to observe that diiodine was not displaced upon electric current application, as the value of conductivity is steady over time.

Conclusions

In summary, we have presented a novel approach to regulate the molecular organization of rhodanine-containing π-conjugated compounds. Our study demonstrates that I_2 can interact at the molecular level, forming stable adducts through interaction with the rhodanine thiocarbonyl terminal groups. Furthermore, preliminary study on the electrical conductivity of single crystals suggests that the molecular arrangement in **BTR·I$_2$** leads to an enhancement of the flow of electric current. Therefore, the following conclusions can be drawn:

(1) I_2 can be used as a solid additive to tailor the molecular organization of rhodanine-containing π-conjugated thiophene derivatives.

(2) The diiodine adduct undergoes a reduction in the HOMO–LUMO energy gap compared to the pristine compound.

(3) FT-Raman spectroscopy represents an effective and fast non-destructive approach to reveal the coordination of diiodine and can therefore be used in semiconductors to verify the adduct formation and its strength in the absence of a single crystal X-ray diffraction analysis, in particular when non-crystalline materials are considered.

(4) Finally, DFT calculations can model both the CT/σ-hole interaction between the Lewis donor and diiodine and the XB intermolecular interactions. In this context, neglecting dispersion effects, two concurrent interpretation models for σ-hole interactions have been proposed, *i.e.* a MO-mixing approach, consisting of a partial charge-transfer from a nucleophile (Lewis base) to an electrophile (Lewis acid), or a noncovalent σ-hole interpretation based on the topology of electrostatic potential. Energy decomposition schemes have shown that both aspects contribute to XB and ChB interactions. As previously shown for different systems showing XB and ChB interactions involving chalcogen donors interacting with dihalogens/interhalogens the two models converge to the same conclusions, with the depletion areas of electrostatic potential (σ-holes) being topologically related to the direction of antibonding natural orbitals.

The case study of **BTR**/**BTR**·$\mathbf{I_2}$ shows for the first time the role played by the introduction of chalcocarbonyl groups in π-conjugated derivatives in the formation of supramolecular architectures based on XB/ChB interactions capable of extending the dimensionality of their lattice, reducing the HOMO–LUMO energy gap, and ultimately increasing their semiconducting behaviour.

These results pave the way for the development of novel processing methods that can be directly applied to SM semiconductors, facilitating the fabrication of optoelectronic devices, such as organic solar cells based on non-fullerene small-molecule acceptors, organic field-effect transistors (OFETs), and organic memory devices (OMDs).

Data availability

The authors confirm that the data supporting the findings of this study are available within the article and/or its ESI.†

Conflicts of interest

There are no conflicts to declare.

Acknowledgements

G. S. would like to thank PON Ricerca e Innovazione (annualità 2014-2020, grant no. DOT1304455-2), Fondazione di Sardegna (annualità 2020, FdS grant no. F75F21001250007) and the Italian Ministry of University and Research (MUR) (National Recovery and Resilience Plan (NRRP) funded by the European Union – Next Generation EU; annualità 2022, grant no. P2022ZHBZE) for the financial support. MA, MCA, VL, and AP acknowledge the Ministero per l'Ambiente e la Sicurezza Energetica (MASE; formerly Ministero della Transizione Ecologica, MITE) – Direzione generale Economia Circolare for funding (RAEE – Edizione 2021). M. A. acknowledges the CINECA award under the ISCRA initiative, for the availability of high-performance computing resources and support (project ChWEEE, HP10CDTEF0). We acknowledge the CeSAR (Centro Servizi di Ateneo per la Ricerca) of the University of Cagliari, Italy for providing access to the SC-XRD facility.

Notes and references

1 M. Sawatzki-Park, S. Wang, H. Kleemann and K. Leo, Highly Ordered Small Molecule Organic Semiconductor Thin-Films Enabling Complex, High-Performance Multi-Junction Devices, *Chem. Rev.*, 2023, **123**, 8232–8250.
2 S. Fratini, M. Nikolka, A. Salleo, G. Schweicher and H. Sirringhaus, Charge transport in high-mobility conjugated polymers and molecular semiconductors, *Nat. Mater.*, 2020, **19**, 491–502.
3 K. Gu and Y. Loo, The Polymer Physics of Multiscale Charge Transport in Conjugated System, *J. Polym. Sci., Part B: Polym. Phys.*, 2019, **57**, 1559–1571.
4 K. Kim, H. Yu, H. Kang, D. J. Kang, C. Cho, H. Cho, J. H. Oh and B. J. Kim, Influence of intermolecular interactions of electron donating small molecules on their molecular packing and performance in organic electronic devices, *J. Mater. Chem. A*, 2013, **1**, 14538–14547.
5 F. Chen, Y. Wang, W. Zhang, T. Tian, B. Bai, H. Wang, F. Bai and M. Li, Role of Intermolecular Interactions in Molecular Packing of Alkoxy-Substituted Bis-1,3,4-oxadiazole Derivatives, *Cryst. Growth Des.*, 2019, **19**, 6100–6113.
6 M. Zhu, P. Li, J. Li and T. Lei, Molecular packing and film morphology control in organic electrochemical transistors, *Mol. Syst. Des. Eng.*, 2022, **7**, 6–20.
7 P. A. Banks, A. M. Dyer, A. C. Whalley and M. T. Ruggiero, Side-chain torsional dynamics strongly influence charge transport in organic semiconductor, *Chem. Commun.*, 2022, **58**, 12803–12806.
8 J. Chen, W. Zhang, L. Wang and G. Yu, Recent Research Progress of Organic Small-Molecule Semiconductors with High Electron Mobilities, *Adv. Mater.*, 2023, **35**, 2210772.
9 J. Yi, G. Zhang, H. Yu and H. Yan, Advantages, challenges and molecular design of different material types used in organic solar cell, *Nat. Rev. Mater.*, 2024, **9**, 46–62.
10 X. Li, X. Kong, G. Sun and Y. Li, Organic small molecule acceptor materials for organic solar cells, *eScience*, 2023, **3**, 100171.
11 B. Kan, Y. Kan, L. Zuo, X. Shi and K. Gao, Recent progress on all-small molecule organic solar cells using small-molecule nonfullerene acceptors, *InfoMat*, 2021, **3**, 175–200.
12 R. Zhoul, Z. Jiang, C. Yang, J. Yu, J. Feng, M. A. Adil, D. Deng, W. Zou, J. Zhang, K. Lu, W. Ma, F. Gao and Z. Wei, All-small-molecule organic solar cells with over 14% efficiency by optimizing hierarchical morphologies, *Nat. Commun.*, 2019, **10**, 5393.
13 J. Ahn, *et al.*, Simple and Versatile Non-Fullerene Acceptor Based on Benzothiadiazole and Rhodanine for Organic Solar Cells, *ACS Appl. Mater. Interfaces*, 2019, **11**, 30098–30107.
14 C. Yan, S. Barlow and Z. Wang, *et al.*, Non-fullerene acceptors for organic solar cells, *Nat. Rev. Mater.*, 2018, **3**, 18003.

15 S. Shoaee, A. L. Sanna and G. Sforazzini, Elucidating Charge Generation in Green-Solvent Processed Organic Solar Cells, *Molecules*, 2021, **26**, 7439.
16 Z. Zhang, J. Yuan, Q. Wei and Y. Zou, Small-Molecule Electron Acceptors for Efficient Non-fullerene Organic Solar Cells, *Front. Chem.*, 2018, **6**, 414.
17 X. Yao, W. Shao, X. Xiang, W. Xiao, L. Liang, F. Zhao, J. Lingd, Z. Lu, J. Li and W. Li, Side chain engineering on a small molecular semiconductor: Balance between solubility and performance by choosing proper positions for alkyl side chains, *Org. Electron.*, 2018, **61**, 56–64.
18 A. Khot and B. M. Savoie, How side-chain hydrophilicity modulates morphology and charge transport in mixed conducting polymers, *J. Polym. Sci.*, 2022, **60**, 610–620.
19 I. E. Kuznetsov, *et al.*, Tailoring the charge transport characteristics in ordered small-molecule organic semiconductors by side-chain engineering and fluorine substitution, *Phys. Chem. Chem. Phys.*, 2022, **24**, 16041–16049.
20 P. J. W. Sommerville, A. H. Balzer, G. Lecroy, L. Guio, Y. Wang, J. W. Onorato, N. A. Kukhta, X. Gu, A. Salleo, N. Stingelin and C. K. Luscombe, *ACS Polym. Au*, 2023, **3**, 59–69.
21 Y. He, N. A. Kukhta, A. Marks and C. K. Luscombe, The effect of side chain engineering on conjugated polymers in organic electrochemical transistors for bioelectronic applications, *J. Mater. Chem. C*, 2022, **10**, 2314–2332.
22 R. Datt, Suman, A. Bagui, A. Siddiqui, R. Sharma, V. Gupta, S. Yoo, S. Kumar and S. P. Singh, Effectiveness of solvent vapor annealing over thermal annealing on the photovoltaic performance of non-fullerene acceptor based BHJ solar cells, *Sci. Rep.*, 2019, **9**, 8529.
23 T. Shan, Y. Zhang, Y. Wang, Z. Xie, Q. Wei, J. Xu, M. Zhang, C. Wang, Q. Bao, X. Wang, C.-C. Chen, J. Huang, Q. Chen, F. Liu, L. Chen and H. Zhong, Universal and versatile morphology engineering via hot fluorous solvent soaking for organic bulk heterojunction, *Nat. Commun.*, 2020, **11**, 5585.
24 H. Liao, C. Ho, C. Chang, M. Jao, S. B. Darling and W. Su, Additives for morphology control in high-efficiency organic solar cells, *Mater. Today*, 2013, **16**, 326–336.
25 H. Lin, X. Yao, M. Li, X. Yu, X. Du, G. Yang, C. Zheng and S. Tao, Volatile Solvent Additives Enabling High-Efficiency Organic Solar Cells without Thermal Annealing, *ACS Appl. Energy Mater.*, 2022, **5**, 15529–15537.
26 Y. Jiang and Z. Li, The effect of additives on the morphology of organic solar cells: A brief review, *Synth. Met.*, 2023, **299**, 117480.
27 M. Choi, H. Jeong, J. Lee, Y. Choi, I. Kim, D. Kim, H. Kang and S. Jang, Non-halogenated and non-volatile solid additive for improving the efficiency and stability of organic solar cells, *J. Mater. Chem. A*, 2024, **12**, 8963–8971.
28 Y. Ma, Y. Zhang and H. Zhang, Solid additives in organic solar cells: progress and perspective, *J. Mater. Chem. C*, 2022, **10**, 2364–2374.
29 S. Yoon, J. Cho, S. H. Yu, Hae J. Son and D. S. Chung, Effects of iodine doping on small molecule organic semiconductors for high charge carrier mobility and photoconductivity, *Org. Electron.*, 2016, **34**, 28e32.
30 C. J. Boyle, *et al.*, Tuning charge transport dynamics via clustering of doping in organic semiconductor thin films, *Nat. Commun.*, 2019, **10**, 2827.
31 M. C. Aragoni, M. Arca, F. A. Devillanova, A. Garau, F. Isaia, V. Lippolis and G. Verani, Charge-transfer adducts between donors containing chalcogens (S and Se) and di-iodine: solution studies, *Coord. Chem. Rev.*, 1999, **184**, 271–290.
32 P. Politzer, J. S. Murray and T. Clark, Halogen bonding and other sigma-hole interactions: a perspective, *Phys. Chem. Chem. Phys.*, 2013, **15**, 11178–11189.
33 M. C. Aragoni, M. Arca, V. Lippolis, A. Pintus, Y. Torubaev and E. Podda, A structural approach to the strength evaluation of linear chalcogen bonds, *Molecules*, 2023, **28**, 3133.
34 A. Vilsmeier and A. Haack, Über die Einwirkung von Halogenphosphor auf Alkyl-formanilide. Eine neue Methode zur Darstellung sekundärer und tertiärer p-Alkylaminobenzaldehyde, *Ber. Dtsch. Chem. Ges.*, 1927, **60**, 119–122.
35 K. van Beurden, S. de Koning, D. Molenndijk and J. van Schijndel, The Knoevenagel reaction: review of the unfinished treasure map to forming carbon–carbon bonds, *Green Chem. Lett. Rev.*, 2020, **13**, 349–364.
36 M. C. Aragoni, M. F. Cherchi, V. Lippolis, A. Pintus, E. Podda, A. M. Z. Slawin, J. D. Woollins and M. Arca, Self-Assembly of Supramolecular Architectures Driven by σ-Hole Interactions: A Halogen-Bonded 2D Network Based on a Diiminedibromido Gold(III) Complex and Tribromide Building Blocks, *Molecules*, 2022, **27**, 6289.
37 H. Svensson and L. L. Kloo, Synthesis, Structure, and Bonding in Polyiodide and Metal Iodide−Iodine Systems, *Chem. Rev.*, 2003, **103**, 1649–1684.
38 F. van Bolhuis, P. B. Koster and T. Migchelsen, Refinement of the crystl structure of iodine at 110°K, *Acta Crystallogr.*, 1967, **23**, 90–91.
39 L. Pauling, *The Nature of the Chemical Bond*, 3rd ed., Cornell University Press, Ithaca, New York, 1960.
40 R. Montis, M. Arca, M. C. Aragoni, A. Bauzá, F. Demartin, A. Frontera, F. Isaia and V. Lippolis, Hydrogen- and halogen-bond cooperativity in determining the crystal packing of dihalogen charge-transfer adducts: a study case from heterocyclic pentatomic chalcogenone donors, *CrystEngComm*, 2017, **19**, 4401–4412.
41 M. C. Aragoni, M. Arca, F. A. Devillanova, M. B. Hursthouse, S. L. Huth, F. Isaia, V. Lippolis, A. Mancini, H. R. Ogilvie and G. Verani, Reactions of pyridyl donors with halogens and interhalogens: an X-ray diffraction and FT-Raman investigation, *J. Organomet. Chem.*, 2005, **690**, 1923–1934.
42 W. Holzer, W. F. Murphy and H. J. Bernstein, Resonance Raman Effect and Resonance Fluorescence in Halogen Gases, *J. Chem. Phys.*, 1970, **52**, 399–407.
43 O. Yildirim, A. Tsaturyan, A. Damin, S. Nejrotti, V. Crocellà, A. Gallo, M. R. Chierotti, M. Bonomo and C. Barolo, Quinoid-Thiophene-Based Covalent Organic Polymers for High Iodine Uptake: When Rational Chemical Design Counterbalances the Low Surface Area and Pore Volume, *ACS Appl. Mater. Interfaces*, 2023, **15**, 15819–15831.

44 E. Hullko, T. Kiljunen, T. Kiviniemi and M. Pettersson, From monomer to bulk: Appearance of the Structural Motif of Solid Iodine in Small Clusters, *J. Am. Chem. Soc.*, 2009, **131**, 1050–1056.
45 W. Kiefer and H. J. Bernstein, Resonance Raman spectroscopic study on iodine in various organic solvents: Spectroscopic constants and halfband widths of the I2 vibration, *J. Raman Spectrosc.*, 1973, **1**, 417–431.
46 A. Congeduti, M. Nardone and P. Postorino, Polarized Raman spectra of a single crystal of iodine, *Chem. Phys.*, 2000, **256**, 117–123.
47 M. Bulatova, D. M. Ivanov, J. M. Rautiainen, M. A. Kinzhalov, K.-N. Truong, M. Lahtinen and M. Haukka, Studies of Nature of Uncommon Bifurcated I–I···(I–M) Metal-Involving Noncovalent Interaction in Palladium(II) and Platinum(II) Isocyanide Cocrystals, *J. Phys. Chem. A*, 2019, **123**, 4575–4580.
48 P. D. Boyle, J. Christie, T. Dyer, S. M. Godfrey, I. R. Howson, C. McArthur, B. Omar, R. G. Pritchard and G. Rh Williams, Further structural motifs from the reactions of thioamides with diiodine and the interhalogens iodine monobromide and iodine monochloride: an FT-Raman and crystallographic study, *J. Chem. Soc., Dalton Trans.*, 2000, 3106–3112.
49 M. Arca, M. C. Aragoni, F. A. Devillanova, A. Garau, F. Isaia, V. Lippolis, A. Mancini and G. Verani, Reactions Between Chalcogen Donors and Dihalogens/Interalogens: Typology of Products and Their Characterization by FT-Raman Spectroscopy, *Bioinorg. Chem. Appl.*, 2006, **58937**, 1–12.
50 M. C. Aragoni, M. Arca, C. Caltagirone, C. Castellano, F. Demartin, P. G. Jones, T. Pivetta, E. Podda, V. Lippolis, S. Murgia and G. Picci, Role of the Solvent in the Reactivity of Bis-4-imidazoline-2-selone Derivatives toward I2: An Experimental and Theoretical Approach, *J. Org. Chem.*, 2022, **87**, 15448–15465.
51 M. C. Aragoni, M. Arca, F. Demartin, F. A. Devillanova, A. Garau, F. Isaia, V. Lippolis and G. Verani, DFT calculations, structural and spectroscopic studies on the products formed between IBr and N,N′-dimethylbenzoimidazole-2(3H)-thione and -2(3H)-selone, *Dalton Trans.*, 2005, 2252–2258.
52 C. Adamo and V. Barone, Exchange functionals with improved long-range behavior and adiabatic connection methods without adjustable parameters: The mPW and mPW1PW models, *J. Chem. Phys.*, 1998, **108**, 664–675.
53 A. Schäfer, H. Horn and R. Ahlrichs, Fully optimized contracted Gaussian basis sets for atoms Li to Kr, *J. Chem. Phys.*, 1992, **97**, 2571–2577.
54 F. Weigend and R. Ahlrichs, Balanced basis sets of split valence, triple zeta valence and quadruple zeta valence quality for H to Rn: Design and assessment of accuracy, *Phys. Chem. Chem. Phys.*, 2005, **7**, 3297–3305.
55 L. E. Roy, P. J. Hay and R. L. Martin, Revised Basis Sets for the LANL Effective Core Potentials, *J. Chem. Theory Comput.*, 2008, **4**, 1029–1031.
56 G. Cavallo, P. Metrangolo, R. Milani, T. Pilati, A. Priimagi, G. Resnati and G. Terraneo, The halogen bond, *Chem. Rev.*, 2016, **116**, 2478–2601.
57 Y. Zhang and W. Wang, Theoretical rationale for the role of strong halogen bond in the design of organic semiconductor materials, *Comput. Theor. Chem.*, 2021, **1194**, 113074.
58 L. J. McAllister, C. Präsang, J. P.-W. Wong, R. J. Thatcher, A. C. Whitwood, B. Donnio, P. O'Brien, P. B. Karadakov and D. W. Bruce, Halogen-bonded liquid crystals of 4-alkoxystilbazoles with molecular iodine: a very short halogen bond and unusual mesophase stability, *Chem. Commun.*, 2013, **49**, 3946–3948.
59 L. de Azevedo Santos, S. C. C. van der Lubbe, T. A. Hamlin, T. C. Ramalho and F. M. Bickelhaupt, A quantitative molecular orbital perspective of the chalcogen bond, *ChemistryOpen*, 2021, **10**, 391–401.
60 V. Oliveira, E. Kraka and D. Cremer, *Phys. Chem. Chem. Phys.*, 2016, **18**, 33031–33046.
61 L. N. Anderson, F. W. Aquino, A. E. Raeber, X. Chen and B. M. Wong, Halogen Bonding Interactions: Revised Benchmarks and a New Assessment of Exchange vs Dispersion, *J. Chem. Theory Comput.*, 2018, **14**, 180–190.
62 A. E. Reed, R. B. Weinstock and F. Weinhold, Natural Population Analysis, *J. Chem. Phys.*, 1985, **83**, 735–746.
63 A. E. Reed and F. Weinhold, Natural localised molecular orbital, *J. Chem. Phys.*, 1985, **83**, 1736–1740.
64 A. E. Reed, L. A. Curtiss and F. Weinhold, Intermolecular interactions from a natural bond orbital, donor-acceptor viewpoint, *Chem. Rev.*, 1988, **88**, 899–926.
65 K. B. Wiberg, Application of the pople-santry-segal CNDO method to the cyclopropylcarbinyl and cyclobutyl cation and to cyclobutane, *Tetrahedron*, 1968, **24**, 1083–1096.
66 J. Luo, Z. Q. Xue, W. M. Liu, J. L. Wu and Z. Q. Yang, Koopmans' theorem for large molecular systems within density functional theory, *J. Phys. Chem. A*, 2006, **110**(43), 12005–12009.
67 X. G. Yang, Y. Zhang, W. Wang and L. F. Ma, Enhanced Optoelectronic Performances of the Cocrystals between 2,2′-Bi (1,8-naphthyridine) and Iodine through Strong Halogen Bonds, *Cryst. Growth Des.*, 2022, **22**, 6863–6869.

